Measurement Report: Development of a portable peroxy radical measurement system and application for diagnosing local ozone formation and transport

Rujia Tang[1,2#], Zelong Zheng[1,2#], Yiming Wang[1,2], Hongxia Liu[1,2], Xiaorui Chen[1,2*], Haichao Wang[1,2]

1 School of Atmospheric Sciences, Sun Yat-sen University, Southern Marine Science and Engineering Guangdong Laboratory (Zhuhai), Zhuhai, 519082, China

2 Guangdong Provincial Observation and Research Station for Climate Environment and Air Quality Change in the Pearl River Estuary, Key Laboratory of Tropical Atmosphere-Ocean System, Ministry of Education, Zhuhai, 519082, China

# These authors contributed equally to this work

Correspondence: X.R.C. (chenxr95@mail.sysu.edu.cn)

Abstract

Atmospheric total peroxy radicals RO_2* (~~$RO_2^* = HO_2 + RO_2$~~$RO_2^* = HO_2 + \sum RO_2$) play central roles in tropospheric chemistry, governing the formation of ozone and secondary aerosols. However, due to their extremely low concentrations and high reactivity, direct observation of RO_2* remains challenging. In this study, a compact instrument for in-situ measurement of RO_2* was developed by combining the Peroxy Radical Chemical Amplification (PERCA) technique with Cavity-Enhanced Absorption Spectroscopy (CEAS). ~~By optimizing operational parameters~~Using a pure HO_2 standard for calibration, the system can achieve a chemical chain length of ~~56~~30 and an optimal detection limit of 0.~~2~~38 pptv (1σ, 3 min), enabling highly sensitive measurements of ambient peroxy radicals. The self-constructed PERCA–CEAS system was successfully deployed in a field campaign during autumn in Zhuhai to observe ambient RO_2*. During the observation period, the mean daytime RO_2* was 31.11 ± 18.87 pptv, which resulted in an average $P(O_3)$ of 14.41 ± 17.04 ppbv~~·~~ h~~$^{-1}$~~. The comparison of O_3 variation and derived $P(O_3)$ indicates that the daytime ozone enhancement in Zhuhai was primarily driven by local photochemical production, while

regional transport acted mainly as an export effect. Our results demonstrate that a compact PERCA–CEAS system is capable of ambient RO_2* measurements and suggest the need of diagnosing O_3 formation pattern with the constraint of high time-resolution RO_2* concentration.

Short Summary

This study developed a portable measurement system based on cavity-enhanced absorption spectroscopy, enabling highly sensitive online monitoring of total peroxy radicals in the atmosphere. The system is compact and was successfully deployed in a field campaign in Zhuhai during autumn. The results indicate that daytime ozone enhancement in this region was primarily driven by local photochemical production, while regional transport mainly played an export role.

1. Introduction

In the troposphere, total peroxy radicals RO_2* ($RO_2^* = HO_2 + \sum RO_2$) are key reactive species that drive photochemical reaction chains in the atmosphere (Monks, 2005). The production and recycling of RO_2* determine both the persistence and efficiency of photochemical reactions. The continual regeneration of NO_2 through radical–NOx chain reactions sustains ozone production and leads to its accumulation (Orlando and Tyndall, 2012; Wang et al., 2022). Moreover, the removal of RO_2* also ~~contribute~~contributes to the formation of secondary organic aerosols (Chen et al., 2022; Ehn et al., 2014; Zou et al., 2025), which plays a crucial role in regional air quality and climate impacts (Liang et al., 2024). Therefore, understanding the spatiotemporal variations of RO_2* is essential for elucidating the evolution of regional atmospheric oxidation capacity and assessing pollution formation potential.

Significant advancements have been made in atmospheric peroxy radical measurement techniques over the past few decades, primarily categorized into two technological pathways: direct and indirect measurements (Gao et al., 2023). The microwave-induced electron spin resonance (MIESR) method identifies radicals through the resonance of unpaired electrons, providing the most direct evidence of their detection. However, MIESR suffers from low sensitivity and complex operation requirements (Mihelcic et al., 1985, 1990). Indirect measurement techniques detect RO_2* by converting it into measurable species through chemical reactions. For example, the ~~Laser-Induced Fluorescence~~laser-induced fluorescence (LIF) technique determines RO_2* concentrations by measuring the OH fluorescence signal generated from the reaction between RO_2* and NO. This method offers high sensitivity and selectivity, whereas it requires a complex setup and is prone to environmental interferences (Lu et al., 2012; Whalley et al., 2013). ~~The Peroxy Radical Chemical Ionization Mass Spectrometry~~The peroxy radical chemical ionization mass spectrometry (PerCIMS) method converts RO_2* into characteristic ions through ion–molecule reactions, enabling highly sensitive and selective quantification of specific radicals (Edwards et al., 2003; Hornbrook et al., 2011). Unlike other ~~approach~~approaches, the peroxy ~~Radical Chemical Amplification~~radical chemical amplification (PERCA) measures RO_2* by amplifying its signal into a large amount of NO_2 through a chain reaction. The

PERCA system has relatively high sensitivity to atmospheric RO_2 radicals. The simple construction and routine maintenance for this system ensure the stable measurement on the field. As a result, PERCA has been widely employed in atmospheric observations (George et al., 2020; Liu and Zhang, 2014; Wei et al., 2023).

In the PERCA system, NO and CO ~~gases~~ are introduced to ~~trigger a series of~~drive chain reactions ~~to convert minor~~that amplify peroxy radicals into detectable NO_2 signals. When sampled air enters the reactor, RO_2 reacts with NO to produce NO_2 and HO_2 ~~and NO_2~~ (R1, R2). The HO_2 then reacts with excess NO to generate OH and NO_2 (R3), and the OH reacts with CO to recycle back to HO_2 (R4). Through this chain reaction cycle, the low-concentration peroxy radical signal is progressively amplified into a high-concentration NO_2 signal (Cantrell et al., 1996). The chemical chain length (CL), defined as the average number of radical propagation cycles occurring within the reactor, serves as a quantitative indicator of the amplification efficiency. The magnitude of CL is governed by the competing rates of radical propagation, termination reactions, and physical losses inside the reactor (Kartal et al., 2010; Reichert et al., 2003). Once the amplified NO_2 concentration (ΔNO_2) is determined, the concentration of RO_2* in ambient air can be derived using the calibrated CL value according to Eq. (1).

$$RO_2 + NO \rightarrow RO + NO_2 \quad (R1)$$

$$RO + O_2 \rightarrow HO_2 + RCHO \quad (R2)$$

$$HO_2 + NO \rightarrow OH + NO_2 \quad (R3)$$

$$OH + CO(+M) \rightarrow HO_2 + CO_2(+M) \quad (R4)$$

$$[RO_2^*] = \frac{\Delta[NO_2]}{CL} \quad (Eq.\,1)$$

Significant progress has been made in peroxy radical chemistry observations and modeling studies in China in recent years. However, most field measurements have been conducted in the major city clusters, such as North China Plain (Ma et al., 2019; Tan et al., 2017, 2018b) , the Yangtze River Delta (Lou et al., 2022; Ma et al., 2022) , and the Pearl River Delta (Lu et al., 2012; Tan et al., 2019; Yang et al., 2022) , while other regions remain underexplored. In addition, RO_2* studies have primarily focused on the urban and inland areas, with limited exploration within the coastal boundary layer (Zhang et al., 2023). The lack of peroxy radical measurements would also constrain direct assessment of photochemical ozone production. In-situ measurements of ambient RO_2* provide a direct basis for calculating local $P(O_3)$, as previous studies

have demonstrated that observed peroxy radical concentrations enable quantitative assessment of instantaneous ozone production rates and its related chemistry across diverse chemical environments (Sommariva et al., 2010; Thornton et al., 2002). Furthermore, the calculated local $P(O_3)$ combined with the observed O_3 variation provides a powerful means to quantify the contribution of ozone transport (Tan et al., 2021). Therefore, developing portable and high-time-resolution RO_2* measurement techniques and applying them to diverse atmospheric environments are crucial for advancing our understanding of complex photochemical processes in the troposphere.

In recent years, optical techniques such as Cavity Enhanced Absorption Spectroscopy (CEAS) have developed rapidly. In our previous work, we constructed a compact and lightweight CEAS instrument with high temporal and spatial resolution for precise NO_2 measurements (Zheng et al., 2024). Building upon this foundation, the current study integrates CEAS with the PERCA system, enabling portable and stable detection of ambient RO_2* measurements. We utilized this system to conduct observations of RO_2* concentration levels in a coastal area during the autumn. Based on our measurements, the local photochemical $P(O_3)$ was derived and subsequently applied to analyzinganalyze the influence of transport on O_3 under both clean and polluted conditions.

2. Experiment and methods

The design of our instrument emphasizes a balance between detection performance (e.g., sensitivity and accuracy) and portability in the field. The PERCA-CEAS system consists of two major components: a chemical amplification module and an NO_2 detection module. The former converts trace radicals into detectable NO_2 signals, while the latter provides precise quantification of the generated NO_2. The chemical amplification module adopts a single-channel configuration to reduce system complexity and physical size while maintaining measurement accuracy. Although conventional dual-channel PERCA systems can effectively remove background interferences, they require two NO_2 detectors operating in parallel (Chen et al., 2016; Liu and Zhang, 2014), leading to potential discrepancy resulted from optical parameters and flow between two channels. In contrast, the single-channel design offers better

structural compactness and operational stability. The produced NO_2 concentration is measured by a self-built CEAS system, which features compact size (40 cm × 30 cm × 17 cm) and lightweight design (5.80 kg). Detailed information of CEAS is provided in our previous work (Zheng et al., 2024). The overall structure of the PERCA-CEAS system is presented in Figure~~.~~ 1.

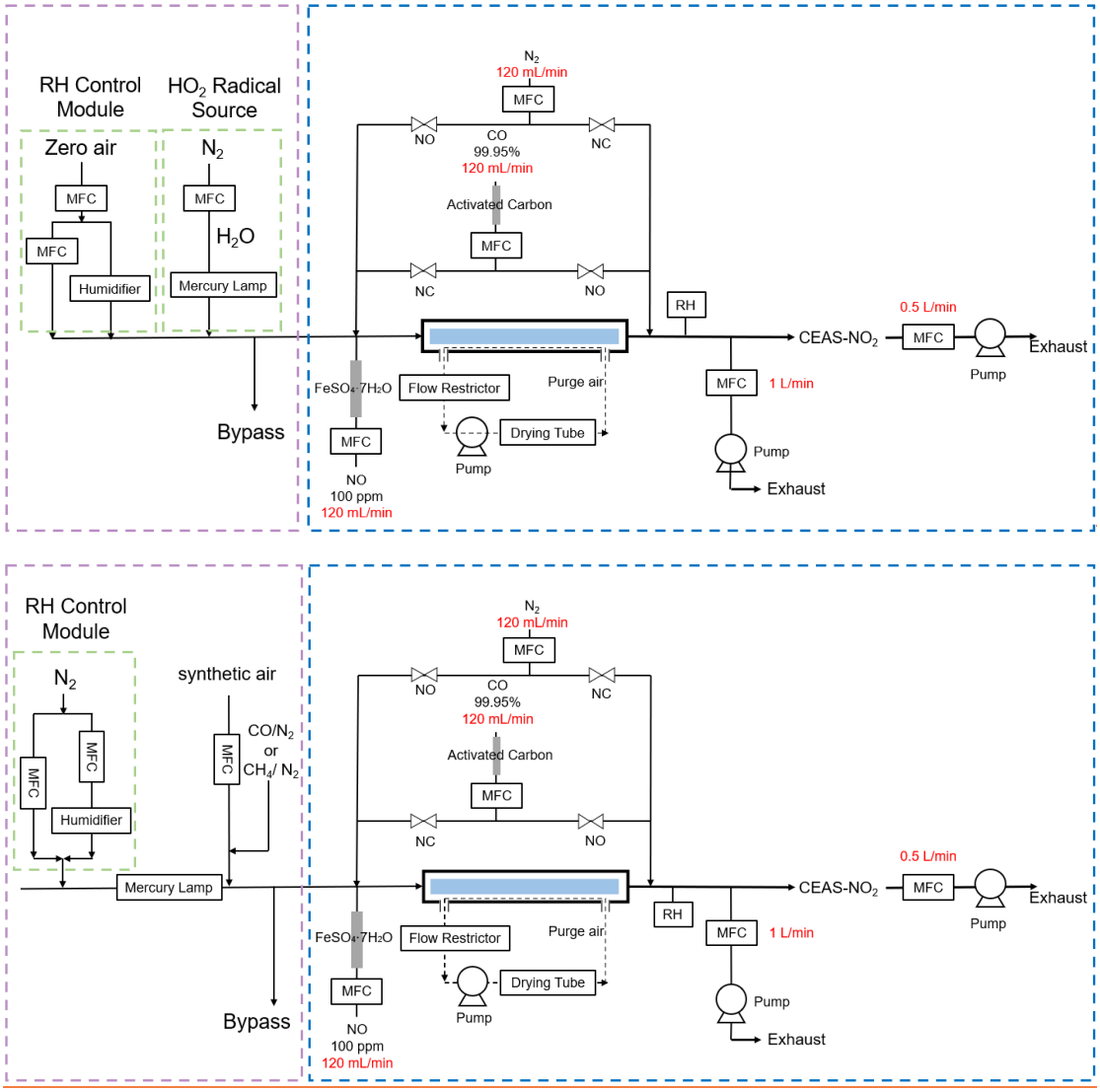

Figure 1. Schematic diagram of the PERCA-CEAS system. The purple dash line portion represents the standard source module, which consists of the standard gas generation unit and the relative humidity (RH) control unit (outlined in green) and is used for calibrating the system chain length. The blue dash line portion represents the measurement module, comprising the chemical amplification unit and the NO_2 detection unit, which together enable the quantification of atmospheric peroxy radicals.

2.1 Chemical amplification module

~~We use~~The NO ~~(8 ppmv)~~ and CO ~~(8 %)~~ gases ~~as reactants~~were injected into the

system accompanied by N_2 as a balancing gas. To ensure gas purity, ~~a series of purification steps were applied before the gases entered the reaction chamber. NO~~the NO (100 ppmv in N_2) was passed through a ferrous sulfate heptahydrate ($FeSO_4 \cdot 7H_2O$) filter to remove trace NO_2 ~~by reduction, while~~ impurities. The flow rate of this NO mixture was regulated at 120 mL/min, achieving a final concentration of 8 ppmv in the reactor. Similarly, high-purity CO gas (99.99%) was ~~purified with~~passed through an activated carbon column to eliminate residual carbonyl compounds ~~from the gas cylinder.~~ before entering the reactor at 120 mL/min, corresponding to a constant concentration of 8% (v/v) during amplification mode. The total system flow was maintained at 1500 mL/min using mass flow controllers, corresponding to a residence time of approximately 3 s in the reaction zone.

To ~~accommodate~~enable automated switching between amplification and background modes in the single-channel configuration, an automatic ~~mode~~valve-switching module ~~was designed to switch between amplification and background modes. In this setup, NO is continuously introduced from the front of the reaction tube, while both N_2 and~~driven by a programmable timer was developed. The flow paths of CO ~~flows~~and N_2 were ~~divided into~~ controlled using four two ~~branches through a three~~-way solenoid ~~valve before entering the system.~~valves, with two valves assigned to each gas line. During the amplification mode, ~~NO and CO are introduced from~~the timer directs CO to the front inlet to initiate the chain reaction with NO, while N_2 is routed to the rear inlet. Conversely, in the background mode, the valve states are toggled so that N_2 is introduced at the front ~~end and N_2 from the rear; during the background mode, NO and N_2 enter from the front while CO is fed from~~and CO is directed to the rear. ~~A programmable timer controls the opening and closing~~By synchronizing the switching of these four ~~solenoid~~ valves, ~~allowing timed switching between~~ the ~~two modes~~system achieves stable and ~~enabling~~automated mode transitions for real-time ~~online~~ detection of peroxy radicals.

Humidity plays a critical role in determining the efficiency of chemical amplification reactions. To control water vapor levels, a Nafion tube dryer (model MD-700-12-F-3, total length 40 cm, effective length 30 cm, ID 1.78cm) was used to remove water vapor and serve as the chemical amplification reaction ~~place~~chamber in the

meantime. To ensure efficient drying and maintain a low-humidity sample stream, a continuous flow of dry purge gas was introduced along the outer side of the Nafion tube. In this work, the dry purge gas was generated by a pump-driven system connected in series with a drying tube filled with indicating silica gel. The gas was first deeply dried through the silica gel column to ensure extremely low moisture content before being circulated from the lower inlet to the upper outlet of the Nafion tube, forming a closed-loop flow. A humidity sensor was installed at the outlet of the sample stream to continuously monitor the relative humidity inside the reaction tube. Through this precise humidity control, the relative humidity ~~on~~during the chemical amplification process was maintained ~~under~~below 20%, ensuring system stability and improving the reliability of the experimental results.

2.2 Chain length calibration

As described in the principle of the chemical amplification method (Eq. (1)), the CL is a key parameter determining the accuracy of peroxy radical measurements. ~~Therefore, the CL of this instrument must be calibrated using a standard peroxy radical source. Calibration is performed with radicals generated on-site. In this study, a HO_2 radical source was generated by photolysis of H_2O using a pen-shaped mercury lamp. Under UV irradiation, H_2O is photolyzed to produce OH and H (R5). The generated H radical can rapidly combine one O_2 to form the hydroperoxyl radical HO_2 through reaction (R6).~~In this work, CL was determined using on-site peroxy radical calibration sources based on water vapor photolysis. A pen-type Hg lamp was used to photolyze H_2O in an N_2 carrier gas (mixture of dry and humidified N_2), producing H atoms and OH radicals (R5). Immediately downstream of the lamp, a mixture of synthetic air and reagent gases (CO/N_2 or CH_4/N_2) was introduced to allow rapid mixing with the photolysis products and reduce radical wall losses. In this configuration, H atoms react with O_2 in the synthetic air to form HO_2 (R6), while the reagent gases control the radical composition. When CO is used as the reagent gas, OH radicals are quantitatively converted to HO_2 (R4), providing a HO_2 calibration source without interference from OH and RO_2 radicals. When CH_4 (150 ppm in N_2) is used instead of CO, OH reacts with CH_4 to form CH_3O_2 (R7), yielding a mixed peroxy radical source containing

approximately 50 % HO_2 and 50 % CH_3O_2 under typical calibration conditions. In all cases, the relative humidity in the calibration flow was adjusted to ~10 %, yielding a stable peroxy radical concentration of ~1–3 ppbv.

$$H_2O + \hbar v \rightarrow OH + H \quad (R5)$$

$$H + O_2 + M \rightarrow HO_2 + M \quad (R6)$$

$$OH + CH_4 + O_2 + M \rightarrow CH_3O_2 + H_2O + M \quad (R7)$$

~~To calibrate the PERCA system, we used the four NO_2 signals detected by the CEAS as calibration references. The calibration procedure comprises four steps as follows. Firstly, when the mercury lamp was turned on, H_2O was photolyzed under UV irradiation to generate the HO_2 source. NO and CO were introduced into the upper inlet of the reaction cell, while N_2 was introduced from the lower inlet. The measured signal, S_1, represents the NO_2 concentration after radical chemical amplification. Secondly, when NO and N_2 were introduced into the upper inlet and CO into the lower inlet, the signal S_2 represents the NO_2 concentration under the radical background mode. Thirdly, the mercury lamp was turned off, and the HO_2 is removed. With NO and CO introduced into the upper inlet and N_2 into the lower inlet, the signal S_3 represents the NO_2 concentration under the chemical amplification mode without radicals. When NO and N_2 were introduced into the upper inlet and CO into the lower inlet, the signal S_4 corresponds to the NO_2 concentration under the background mode without radicals. Based on above measured NO_2 signals (S_1, S_2, S_3 and S_4), the CL can be calculated using Eq. (2). Here, S_2–S_4 represents the NO_2 signal difference produced by the peroxy radicals generated from the standard source under the background mode, reflecting their original concentration level. The S_1–S_3 corresponds to the total NO_2 signal difference obtained under the chemical amplification mode, where the same amount of peroxy radicals is amplified through the reaction cycles. Therefore, the CL can be determined from the ratio of (S_1–S_3) to (S_2–S_4).~~

$$CL = \frac{\Delta NO_2}{[HO_2]} = \frac{S_1 - S_3}{S_2 - S_4} \quad (Eq.2)$$

The CL was determined using four distinct NO_2 signals detected by the CEAS. For the pure HO_2 source, the Hg lamp was switched on and CO was introduced immediately behind the H_2O photolysis zone, with NO at the inlet of Nafion reactor. Under these

conditions, both H atoms and OH from H_2O photolysis were promptly converted to HO_2, then titrated by NO to form NO_2. The resulting NO_2 signal is denoted as S_1 (amplification mode). In the background mode, the lamp remained on while CO was substituted by N_2. The corresponding NO_2 signal, S_2, represents the background mode when HO_2 is only produced by $H+O_2$ pathway. With the lamp off, signal S_3 and S_4 correspond to the amplification and background signals in the absence of radicals, respectively. Thus, ($S_2 - S_4$) represents the HO_2 only produced by $H+O_2$ pathway, whereas ($S_1 - S_3$) corresponds to the chain-amplified NO_2 signal from HO_2 produced via both the $H + O_2$ and OH + CO pathways. The CL is then obtained from these four signals using Eq. (2). The mixed HO_2–CH_3O_2 standard was generated by introducing CH_4 only during the S_1 (amplification) measurement and was used to verify the instrument response to organic peroxy radicals relative to HO_2 under otherwise identical conditions.

$$CL = \frac{\Delta NO_2}{[HO_2]} = \frac{S_1 - S_3}{2(S_2 - S_4)} \quad (Eq.\,2)$$

3. Results and discussion

3.1 Dependence of the CL on Reaction Conditions

The CL is influenced by several factors, including the concentrations of reactive gases, reaction time, relative humidity, and wall losses (Liu and Zhang, 2014). To investigate the response of CL to these parameters in our PERCA-CEAS system, we measured the CL under a series of controlled conditions using a pure HO_2 radical standard source, specifically by varying NO concentrations and RH levels. The CL measurement was repeated at least five ~~time~~times for each condition. For the subsequent experiments, the CO concentration was fixed at 8%, which is sufficiently high to sustain efficient HO_2 production while remaining within safe limits of CO (explosion range: 12.5–74.2%).

To assess how NO concentration influences CL, we conducted a series of experiments under varying NO levels while keeping the relative humidity fixed at 10%. As shown in Figure 2(a), CL increases steadily with increasing NO concentration and reaches its maximum when NO is 8 ppm. Considering both measurement efficiency

and system economy, 8 ppm was chosen as the optimal NO concentration for instrument operation.

At high RH, water vapor on the reactor walls enhances the heterogeneous uptake of RO_2 and HO_2 and promotes HOx-terminating reactions, thereby suppressing chain propagation and shortening the CL (Mihele et al., 1999; Yang et al., 2019)~~.~~. To quantify the effect of RH on the CL, a custom-built humidifier was used to control the flow rate of the humidified gas, thereby generating HO_2 sources at different RH levels (10%–50%). The relative humidity of the sample gas was monitored by a temperature–humidity sensor installed downstream of the Nafion reaction tube. The experimental results, presented in Figure 2(b), demonstrate a substantial decrease in CL as the RH increases. Specifically, when the relative humidity (RH) of the sample gas passing through the Nafion dryer reaches 50%, the chain length drops by more than ~~66~~50.1%, a reduction that severely compromises the sensitivity required for accurate field RO_2* measurements. Consequently, to ensure optimal measurement performance, the RH of the airflow entering the amplification zone is strictly controlled to remain below 20% during field campaigns, corresponding to 45% RH in ambient air.

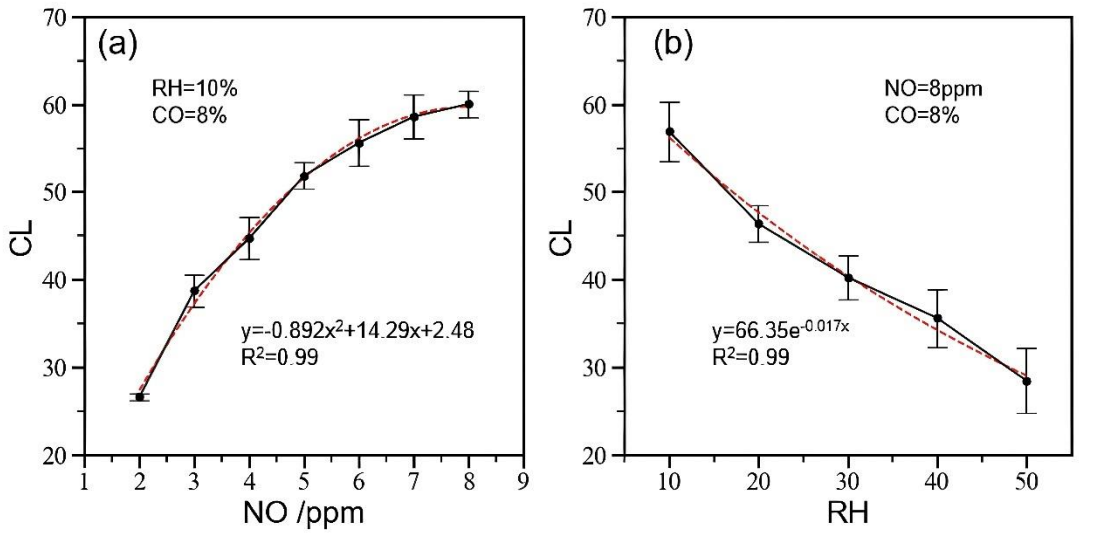

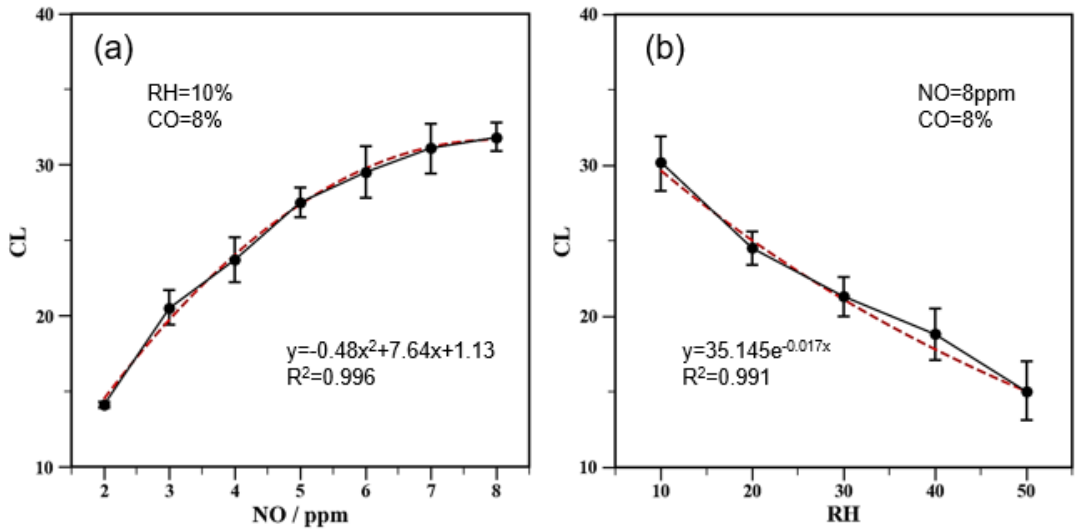

Figure 2. (a) Relationship between the CL and NO concentration under conditions of 10% RH and 8% CO concentration. (b) Variation of CL with RH at a fixed NO concentration of 8 ppm and CO concentration of 8%. (Error bars represent the standard deviation of five independent measurements.)

~~The optimal CL for the PERCA-CEAS measurement system (under RH=10%, NO=8ppm, CO=8%) was determined to be 56±4. Some previous studies have reported much higher CL: for example, (Green et al., 2003) reported CL≈260 for a single-channel ground system, and (Wood and Charest, 2014) found CL = 208±25 under idealized laboratory conditions (at 0% RH). In comparison, the chain length determined in our study remains consistent with values obtained from PERCA systems that employ similar CRDS or CEAS system, where effective CL commonly fall within the range of 44–91 (Duncianu et al., 2020; George et al., 2020; Horstjann et al., 2014). Overall, these results indicate that the CL of our PERCA–CEAS system is reasonable and provides sufficient sensitivity for atmospheric RO_2* measurements.~~

The optimal CL for the PERCA-CEAS measurement system was determined to be 30±2 under the conditions of RH = 10%, NO = 8 ppm, and CO = 8% based on the pure HO_2 calibration. Calibration using a mixed radical source consisting of 50% HO_2 and 50% CH_3O_2 yielded a CL of 24±1 under the same conditions. As summarized in Table 1, the obtained CL is lower than values reported in most previous PERCA studies, which were typically above 50 and occasionally exceeded 200 (George et al., 2020; Wood and Charest, 2014). The differences in CL are primarily attributed to wall loss of HO_2 radicals due to reactor material, reactor design and working pressure. Although the

obtained CL is relatively low compared with these PERCA instruments, the results demonstrate that the developed PERCA-CEAS system provides stable and reliable sensitivity for atmospheric RO_2* measurements.

Table 1. Summary of performance for reported PERCA measurement systems

Measurement System	Channel Configuration	Calibration Source	CL	LOD	Uncertainty	Pressure (mbar)	Reference
PERCA-luminox	Single	CH_3O_2	200-260	2 pptv	40%	400 ~ 1000	(Green et al., 2003)
PERCA-luminol	Dual	HO_2 50%HO_2+50%CH_3O_2	45±7	3±2 pptv (3σ)	/	200	(Kartal et al., 2010)
PERCA-luminol	Dual	HO_2 50%HO_2+50%CH_3O_2	88±17 64±18	3 pptv (1σ)	/	300	(Horstjann et al., 2014)
PERCA-CRDS	Dual	HO_2	150±50	10 pptv (3σ)	/	1000	(Liu et al., 2009)
PERCA-CRDS	Dual	HO_2 CH_3O_2	200 180	4 pptv (3σ)	/	1000	(Liu and Zhang, 2014)
PERCA-CRDS	Dual	HO_2 50%HO_2+50%CH_3O_2	62 ± 9	< 2 pptv	15%	200 ~ 350	(George et al., 2020)
PERCA-CRDS	Dual	HO_2 RO_2*	55	0.9 pptv (3σ)	/	1000	(Duncianu et al., 2020)
PERCA-CAPS	Dual	$CH_3C(O)O_2$ CH_3O_2	168±20	0.6 pptv (1σ, 60s)	25%	1000	(Wood and Charest, 2014)
ECHAMP-CAPS	Dual	$CH_3C(O)O_2$ CH_3O_2	17	2.5 pptv (1σ, 90s)	27%	1000	(Wood et al., 2017)
PERCA-IBBCEAS	Dual	HO_2	91±11	0.9 pptv (1σ)	16-20%	1000	(Chen et al., 2016)
PERCA-CEAS	Single	HO_2 50%HO_2+50%CH_3O_2	30±2 24±1	0.38 pptv (1σ)	18.4-25.7%	1000	This work

3.2 Detection Limit and Measurement Uncertainty

In the PERCA–CEAS system, the concentration of RO_2* is determined by converting it into measurable NO_2 through chain reactions with excess NO. Consequently, the overall detection limit of the system depends on both the detection

limit of NO_2 and the CL, as described by Eq. (3). The LOD for the CEAS-NO_2 ~~model~~detector was determined under laboratory conditions by continuously measuring high-purity zero-air for over 5 hours and calculating the standard deviation of blank noise (~~-~~Zheng et al., 2024)~~-~~. At a 3 min time resolution, the LOD of NO_2 was determined to be 11.4 pptv, ~~which yield~~corresponding to a detection limit of 0.~~2~~38 pptv (1σ, 3min) for RO_2~~*.~~*, based on a CL of 30 derived from the pure HO_2 calibration.

~~The overall measurement uncertainty of the system was quantified using the Gaussian error propagation (Eq. (4)). Three major sources contribute to the total uncertainty: (1) NO_2 measurement uncertainty (6%), which includes uncertainties in the absorption cross-section (4%), mirror reflectivity calibration (5%), effective cavity length (0.5%), and pressure measurement (0.1%); (2) CL calibration uncertainty (7%), derived from repeated calibration results (56 ± 4); and (3) uncertainty in radical partitioning (8–14%) (Kartal et al., 2010). Based on these factors, the overall uncertainty in ROx measurement was estimated to be 12–17%, demonstrating the robustness and reliability of the PERCA–CEAS system for RO_2* measurement.~~

~~$$DL(RO_2^*) = \frac{DL(NO_2)}{CL} \quad (3)$$~~

~~$$\frac{\sigma_{RO_2^*}}{RO_2^*} = \sqrt{\left(\frac{\sigma_{NO_2}}{NO_2}\right)^2 + \left(\frac{\sigma_{CL}}{CL}\right)^2 + \left(\frac{\sigma_{Part}}{Part}\right)^2} \quad (4)$$~~

The overall measurement uncertainty of the system was quantified using the Gaussian error propagation (Eq. (4)). Four major sources contribute to the total uncertainty: (1) NO_2 measurement uncertainty (6%), which includes uncertainties in the absorption cross-section (4%), mirror reflectivity calibration (5%), effective cavity length (0.5%), and pressure measurement (0.1%). (2) CL calibration uncertainty (6.7%), derived from repeated calibration results (30 ±2). (3) Uncertainty in radical partitioning. This arises from variability in the relative contributions of HO_2 and CH_3O_2 to total peroxy radicals. Based on the reported HO_2/RO_2 (0.8–1.2) and CH_3O_2/RO_2 (0.85–0.95) ratios from Stone et al., (2010), the mole fraction of CH_3O_2 in total peroxy radicals (f) is estimated to be 0.41–0.54. Under these conditions, the use of an HO_2-based calibration would introduce a systematic bias of 16–22% in the derived RO_2* concentration. (4) PAN interference. The thermal decomposition of PAN represents a potential source of interference, as it releases NO_2 and peroxy radicals that can trigger

additional chemical amplification within the reactor (Liu and Zhang, 2014; Wood and Charest, 2014). Kinetic simulations using the F0AM model (Framework for 0-D Modeling; Wolfe et al., 2016) indicate that 1.0 ppbv PAN results in an equivalent RO_2* signal of 1.95 pptv under our experimental conditions (26.5 °C and an amplification reaction time of 0.15 s). This accounts for 1.3–9.8% of the typical RO_2* levels (20–150 pptv) observed during the campaign. Based on these factors, the overall uncertainty in ROx measurement was estimated to be 18.4-25.7%, demonstrating the robustness and reliability of the PERCA–CEAS system for RO_2* measurement.

$$LOD(RO_2^*) = \frac{LOD(NO_2)}{CL} \quad (Eq.3)$$

$$\frac{\sigma_{RO_2^*}}{[RO_2^*]} = \sqrt{\left(\frac{\sigma_{NO_2}}{[NO_2]}\right)^2 + \left(\frac{\sigma_{CL}}{CL}\right)^2 + \left(\frac{\sigma_{Part}}{Part}\right)^2 + \left(\frac{\sigma_{PAN}}{PAN}\right)^2} \quad (Eq.4)$$

3.3 Field Observation of RO_2*

The instrument has been deployed in a field campaign to evaluate the performance of instrument under real ~~atmosphere~~atmospheric conditions. All instruments are placed on the roof of a six-story building ~~in~~on the campus of Sun Yat-sen University (22°21′06″ N, 113°35′42″ E), which is located ~~in~~on the western shore of the Pearl River Estuary and approximately 15 km from downtown Zhuhai. The observation site mainly received an airmass mixed with vehicle emissions from a traffic artery (~~300m~~300 m) and nearby residential areas. There are no major industrial facilities in the surroundings.

The field observation campaign was conducted from October 26 to November 15, 2024, producing more than 15 days of valid continuous RO_2* radical data. For PERCA-CEAS operation, both the chemical amplification mode and the background mode were set to 90 s in this observation, resulting in a time resolution of 3 min. Ambient temperature and relative humidity were continuously monitored using a temperature–humidity probe (HC2A-SH, ROTRONIC, Switzerland). The concentrations of NO and NO_2 were measured by a commercial chemiluminescence analyzer (Model 42i-TL, Thermo, USA), while O_3 concentrations were obtained using a UV photometric analyzer (Model 49i, Thermo, USA). The mirror reflectivity of the CEAS detector was calibrated before and after the campaign, and the results remained consistent.

Figure 3(a-c) presents the time series of meteorological parameters and major

pollutants during the observation period. Ambient temperature was consistently above 25 °C, with an average value of 28.44 ± 1.5 °C. Due to the coastal meteorological conditions, the RH was relatively high and ~~show~~showed clear diurnal variations—lower during the day and higher at night—ranging from 25% to 85%, with an average of 55.98 ± 12.53%. Low NO and NO_2 concentrations were observed with an average of 0.34 ± 0.81 ppbv and 13.21 ± 4.72 ppbv, respectively, indicating generally weak NOx emissions from traffic at this site. The daily maximum of O_3 concentrations ranged from 54 to 116 ~~to 5.6~~ ppbv ~~with an average of~~, while the overall mean concentration was 44.86 ± 25.03 ppbv, suggesting a moderate level of photochemical pollution during the observation period.–

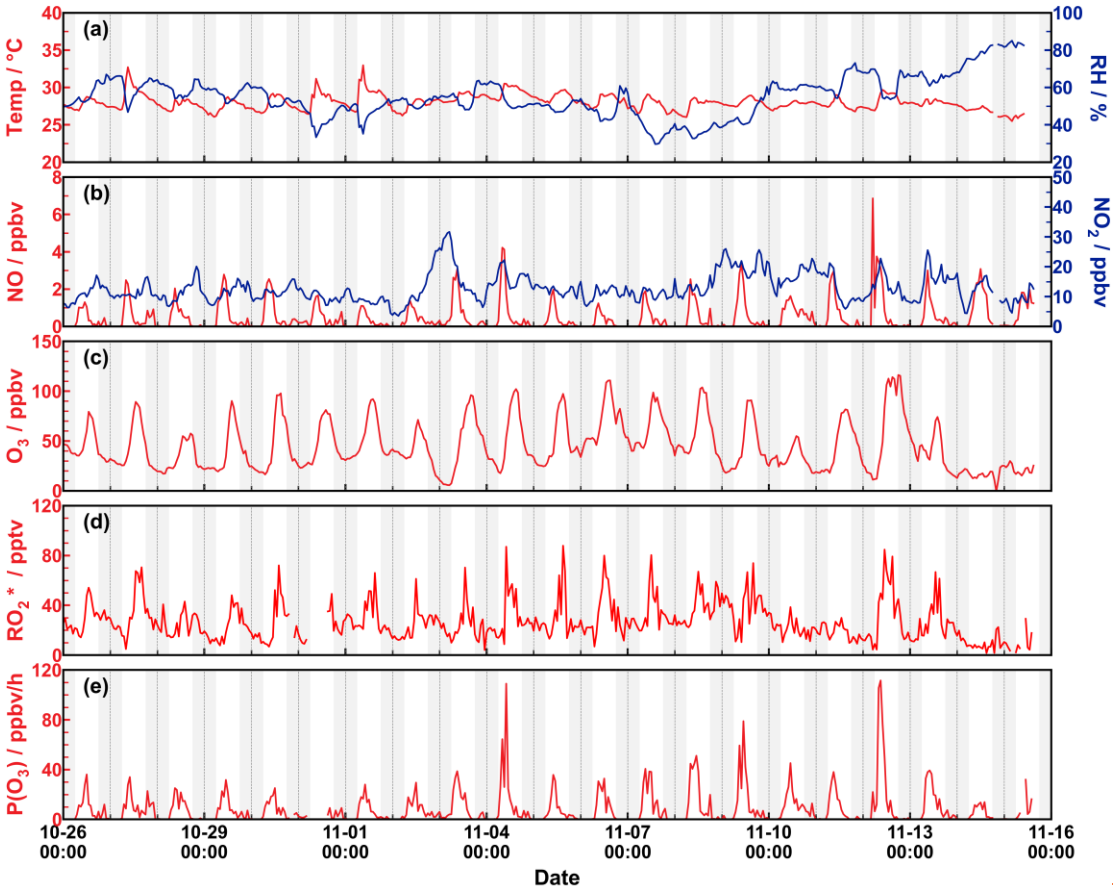

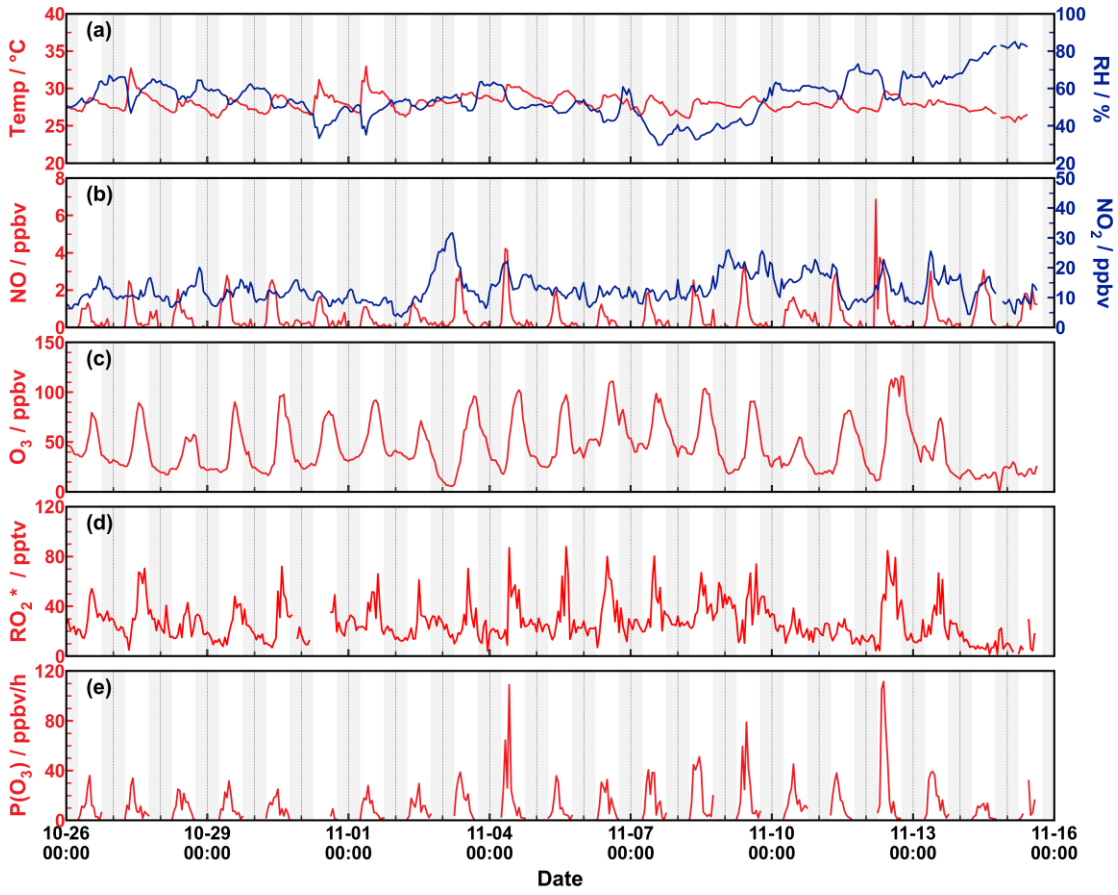

Figure 3. Time series of meteorological parameters (T, RH), major pollutants (O_3, NOx, RO_2*), and daytime P(O_3) (06:00–18:00) during the autumn observation period of 2024, with a temporal resolution of 1 hour.

Compared to previous observation in PRD region, moderate levels of RO_2* were observed with the daily peaks ranging from 48 to 87 pptv (Figure 3d). The RO_2* exhibited a pronounced daytime peak, with an average of 51.3 pptv at around 13:00, and deceased to around 20 pptv at night (Figure 4a). The relatively high level of RO_2* at night indicates the presence of a nighttime peroxy radical source possibly due to NO_3 chemistry oxidation. We found that the average NO_3 production rate (P(NO_3)) at night during the campaign was approximately 1.4 ppbv·h^{-1}, higher than the reported warm-season mean of 1.07 ± 0.38 ppbv·h^{-1} over China (Wang et al., 2023a), indicating active nighttime NO_3 chemistry at this site.~~, which can be evidenced by the occasional increase of RO_2* after sunset.~~ The daytime average of RO_2* (31.11 pptv) was 1-3 times higher than those reported in most suburban areas, while it was lower than those observed in urban areas (Tan et al., 2019; Wang et al., 2023).

In addition, our observed RO_2* exhibited nonlinear response to NO variation

(Figure 4b). At low NO levels, RO_2* increases with NO by promoting the RO_2*–HOx propagation cycle. Once NO exceeds about 1 ppbv, the excess NO rapidly converts peroxy radicals into termination products (e.g., organic nitrates), thus interrupting the radical chain cycle and leading to a decline in RO_2* concentrations (Thornton et al., 2002). The turning point of NO response is higher than that reported in previous studies (Ma et al., 2022; Wei et al., 2023; Yang et al., 2022). ~~High turning point could be attributed to elevated VOCs reactivity due to distinct VOC components supporting more rapid RO_2* production at this coastal~~This behavior is consistent with the elevated VOC reactivity inferred for studies conducted near our observation site. Studies at nearby coastal sites (e.g., Da Wan Shan Island) have reported high oxidative capacity associated with strong VOC consumption and enhanced radical cycling (Sun et al., 2024), while the dense vegetation in the Pearl River Delta contributes substantial biogenic VOC emissions (e.g., isoprene) (Situ et al., 2013; Wang et al., 2023c). Collectively, these factors contribute to sustaining propagation cycles of RO_2 radical and shift the turning point of the NO dependence of RO_2* concentration higher at our site.

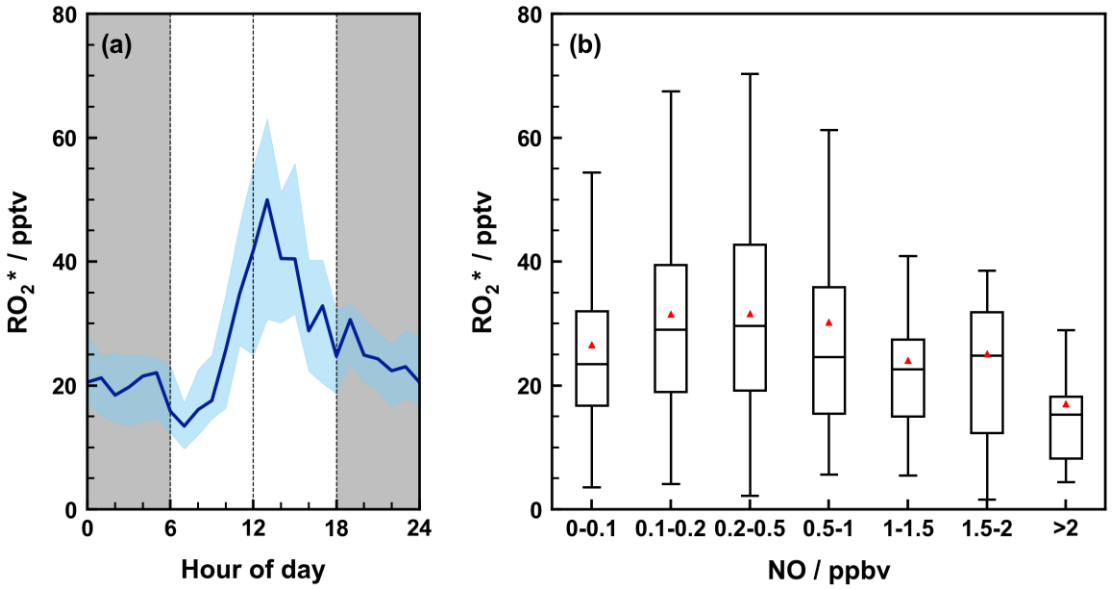

Figure 4. Diurnal variation of RO_2* and its dependence on NO concentration. (a) Average diurnal variation of RO_2* during the observation period. The gray shaded areas indicate nighttime (18:00–06:00), the dark line represents the median values, and the light blue shading shows the interquartile range (25th–75th percentile). (b) Boxplots of RO_2* distributions under different NO concentration ranges. The black line inside each box denotes the median, and the red triangles indicate the mean RO_2* values for each NO interval.

3.4 Local production and Transport of Ozone

The instantaneous ozone production rate is driven by peroxy radical chain propagation involving the reaction of NO and RO_2* (Griffith et al., 2016)~~.~~. Therefore, we calculated $P(O_3)$ based on measured RO_2* using Eq. 5. Since the rate constants of HO_2 + NO and RO_2 + NO reactions are similar (the difference between k_{NO+HO2} and k_i is less than 10%) (Orlando and Tyndall, 2012), an effective rate constant k_{eff} is adopted for the calculation, which is typically approximated by the value of k_{NO+HO2} (Anderson et al., 2019). The photochemical loss of ozone $D(O_3)$ is calculated using Eq. 6, including the photolysis, reactions with OH and HO_2, and the reaction of NO_2 with OH (Tan et al., 2021). Here, $D(O_3)$ was derived using kinetic rate constants together with observed mean concentrations (and representative literature values for unmeasured species) under 298 K and 1 atm. Using the typical conditions ($j(O^1D)=1.0\times10^{-5}$ s^{-1}, $OH=1.0\times10^6$ cm^{-3}, NO=10 ppbv, O_3=40 ppbv, $HO_2\approx$15 pptv), $D(O_3)$ was estimated to be ~0.70 ppbv~~·~~h^{-1}, accounting for only ~5% of $P(O_3)$. Therefore, $P(O_3)$ can be approximated as $P(O_3)_{net}$. Considering uncertainties associated with RO_2* measurements (18.4-25.7%), the approximation of k_{eff} (~10%), and upper limit of $D(O_3)$ level (5%), the overall uncertainty in $P(O_3)_{net}$ was estimated to be 21.5–28.0%.

$$P(O_3) = k_{NO+HO_2}[HO_2][NO] + [NO]\sum_i k_i[RO_2]_i = k_{eff}[RO_2^*][NO] \quad (Eq.5)$$

$$D(O_3) = f_{H_2O}j(O^1D)[O_3] + k_{OH+O_3}[OH][O_3] + k_{HO_2+O_3}[HO_2][O_3] + k_{OH+NO_2}[OH][NO_2] \quad (Eq.6)$$

$$P(O_3)_{net} = P(O_3) - D(O_3) \quad (Eq.7)$$

Substantial variability in $P(O_3)$ was observed during the campaign, with daily peak values ranging from ~~11~~14 to ~~110~~111 ppbv·h^{-1} and a daytime average of 14.41 ± 17.04 ppbv·h^{-1} (Figure~~.~~ 3e). After sunrise, with increasing solar intensity and NO concentrations, photochemical reactions became more active, leading to a rapid increase in $P(O_3)$, which peaked around 10:00 (~27 ppbv·h^{-1}) (Figure~~.~~ 5a). Subsequently, $P(O_3)$ gradually decreased in the afternoon with the weakening solar radiation. We found a sustaining increase of $P(O_3)$ with NO concentration (Figure~~.~~ 5b), suggesting that ozone formation fell within the NOx-limited regime under typical daytime conditions at this site. Similar positive $P(O_3)$–NOx relationships have been reported in both urban and suburban environments — such as the Nashville plume study (Thornton et al., 2002), rural North China field campaigns (Tan et al., 2018a), and recent

observations in Hefei (Yu et al., 2023). The consistent increase of $P(O_3)$ and RO_2* within low NOx levels ~~demonstrate~~demonstrates that the chain propagation for peroxy formation can be enhanced by NO increase and jointly accelerate instantaneous $P(O_3)$.

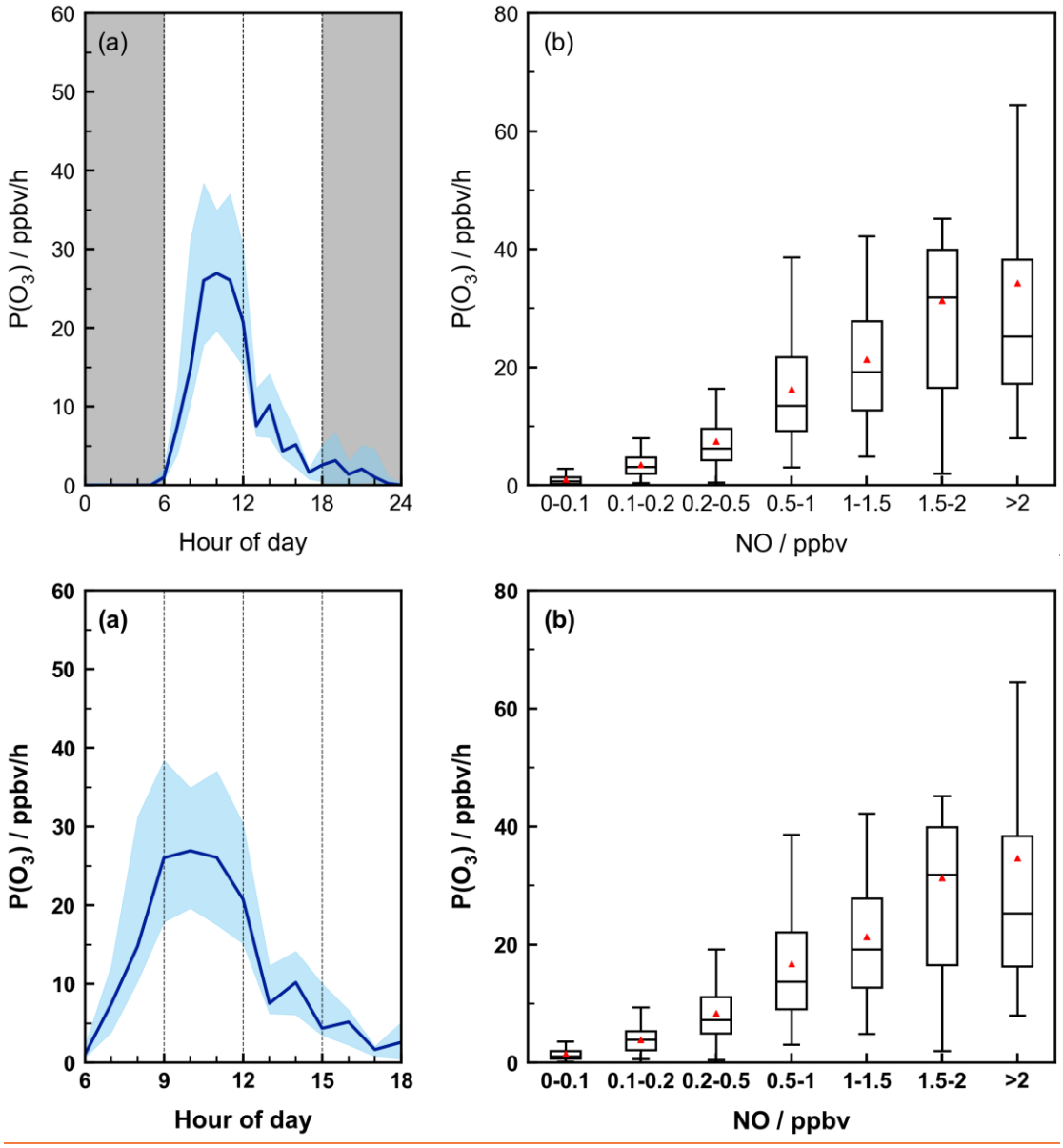

Figure 5. Diurnal variation and NO-dependent distribution of daytime $P(O_3)$. (a) Average diurnal profile of daytime $P(O_3)$ during the observation period. ~~The gray shaded area represents nighttime (18:00–06:00).~~ The dark line denotes the median, and the light blue shading indicates the interquartile range (25th–75th percentile). (b) Box plots of daytime $P(O_3)$ under different NO concentration ranges. The black line inside each box represents the median, and the red triangle marks the mean value within each interval.

We summarized previously reported observations of RO_2*, $P(O_3)$, and related parameters in Table ~~1~~2. The $P(O_3)$ observed in this study was generally higher than

those at low-NO sites such as Wangdu (10.44 ppbv·h^{-1}), San Antonio (4.2 ppbv·h^{-1}), and Hefei (5.91 ppbv·h^{-1}) except for a suburban site in northern China (19.5 ppbv·h^{-1}). Even high-NO sites like Paris (15.8 ppbv·h^{-1}) and Heshan (18.1 ppbv·h^{-1}) showed comparable or slightly higher P(O_3) than our results. This comparison suggests that, despite the moderate RO_2* levels at our site, the instantaneous photochemical ozone production remained considerably strong, pointing to an efficient RO_2*–NOx catalytic cycle in Zhuhai.

Table ~~1~~2. Summary of observed RO_2*, HO_2, NO, O_3, and P(O_3) during the field campaign.

Region	Location	Season, year	RO_2* (pptv)	HO_2 (pptv)	NO (ppbv)	O_3 (ppbv)	P(O_3) (ppbv~~/~~·h^{-1})	References
Suburban	Paris, France	Summer, 2009	5.6	/	4	38	15.8[d]	(Michoud et al., 2012)
Rural	Wangdu, China	Summer, 2014	43.23[a]	19.52[a]	0.72[a]	72.37[a]	10.44[a,c]	(Tan et al., 2017)
Suburban	Heshan,China	Autumn, 2014	17.1	10.2	2.5	42.5	18.1[c]	(Tan et al., 2019)
Urban	San Antonio, USA	Summer, 2017	37[b]	/	0.23[b]	40[b]	4.2[b,c]	(Anderson et al., 2019)
Urban	Guangzhou, China	Autumn, 2018	91.5	/	4.31	31.6	/	~~(Wang et al., 2023)~~(Wang et al., 2023b)
Suburban	Hefei, China	Summer, 2020	27.62	/	0.37	55.19	5.91[c]	(Yu et al., 2023)
Suburban	Huaibei, China	Autumn, 2021	50.34	/	0.3	52.66	19.5[d]	(Wei et al., 2023)
Coastal	Zhuhai, China	Autumn, 2024	31.11	/	0.84	54.44	14.41[c]	This work

Note: All unmarked data represent daytime averages (06:00–18:00).

[a] indicates daytime median values (06:00–16:00);

[b] indicates daytime median values (07:00–20:00);

[c] represents P(O_3) calculated based on the observed peroxy radical concentrations;

[d] represents P(O_3) calculated based on model-simulated peroxy radicals;

"/" represents data not available.

Based on our measurements, we can quantitatively distinguish the relative contributions from local photochemical production and regional transport to surface O_3. Considering the rapid equilibrium between NO_2 and O_3, the variation of odd oxidants (d[Ox]/dt, where Ox = O_3 + NO_2) is used to reflect the combined influence of local photochemical and transport on surface ozone. Therefore, the transport impact can be expressed by $R(O_3)$, which is calculated from the difference between d[Ox]/dt and $P(O_3)_{net}$ as defined in Eq. 8:

$$R(O_3) = \frac{dO_x}{dt} - P(O_3)_{net} \quad (Eq. 8)$$

Here, the sign of $R(O_3)$ indicates the different influences from transport. When $R(O_3) > 0$, regional transport enhances local O_3 concentrations, suggesting that O_3 could be contributed by transport from surrounding regions. Conversely, $R(O_3) < 0$ implies that transport acts as a dilution or export role in regulating the surface ozone.

The contribution from local photochemical production and transport to surface O_3 exhibited distinct patterns under different pollution conditions (Figure 6). We define the polluted days as the maximum O_3 concentration exceeding the national Class I standard of 160 μg/m^3, while the clean periods corresponded to days with a maximum hourly O_3 concentration below 120 μg/m^3. A total of 14 days and 4 days ~~is~~are categorized into polluted and clean periods, respectively. The daytime increase in ozone concentration in Zhuhai was primarily driven by local photochemical production, whereas regional transport generally exhibited an export effect. However, the magnitudes and temporal patterns of their contributions differed significantly between clean and pollution scenarios. The $P(O_3)$ exhibited similar diurnal variations among both polluted and clean days, while polluted periods showed stronger ozone formation than clean periods. Specifically, the peak $P(O_3)$ on polluted days reached ~30 ppbv–·h^{-1}, which was approximately 50% higher than that on clean days (~20 ppbv–·h^{-1}). In contrast to $P(O_3)$, the behavior of $R(O_3)$ on polluted days diverged significantly from that on clean days. Around midday, $R(O_3)$ on polluted days rose rapidly from a negative value to zero and became slightly positive, indicating a suppressed airmass dispersion or even slight import from regional O_3. The distinct transport patterns during polluted days are attributed to frequent coastal wind-field convergence that weakened ventilation. Such

weakening export in the midday facilitated the rapid accumulation of locally produced ozone and contributed to the higher O_3 peaks during polluted days compared to clean days. As a result, the elevated surface ozone on polluted days was resulted from the combined effect of stronger photochemical production and reduced O_3 export ~~in the~~at midday, whereas the $P(O_3)$ was almost offset by the transport effect of O_3 ~~in~~on clean days, leading to flat variation of O_3.

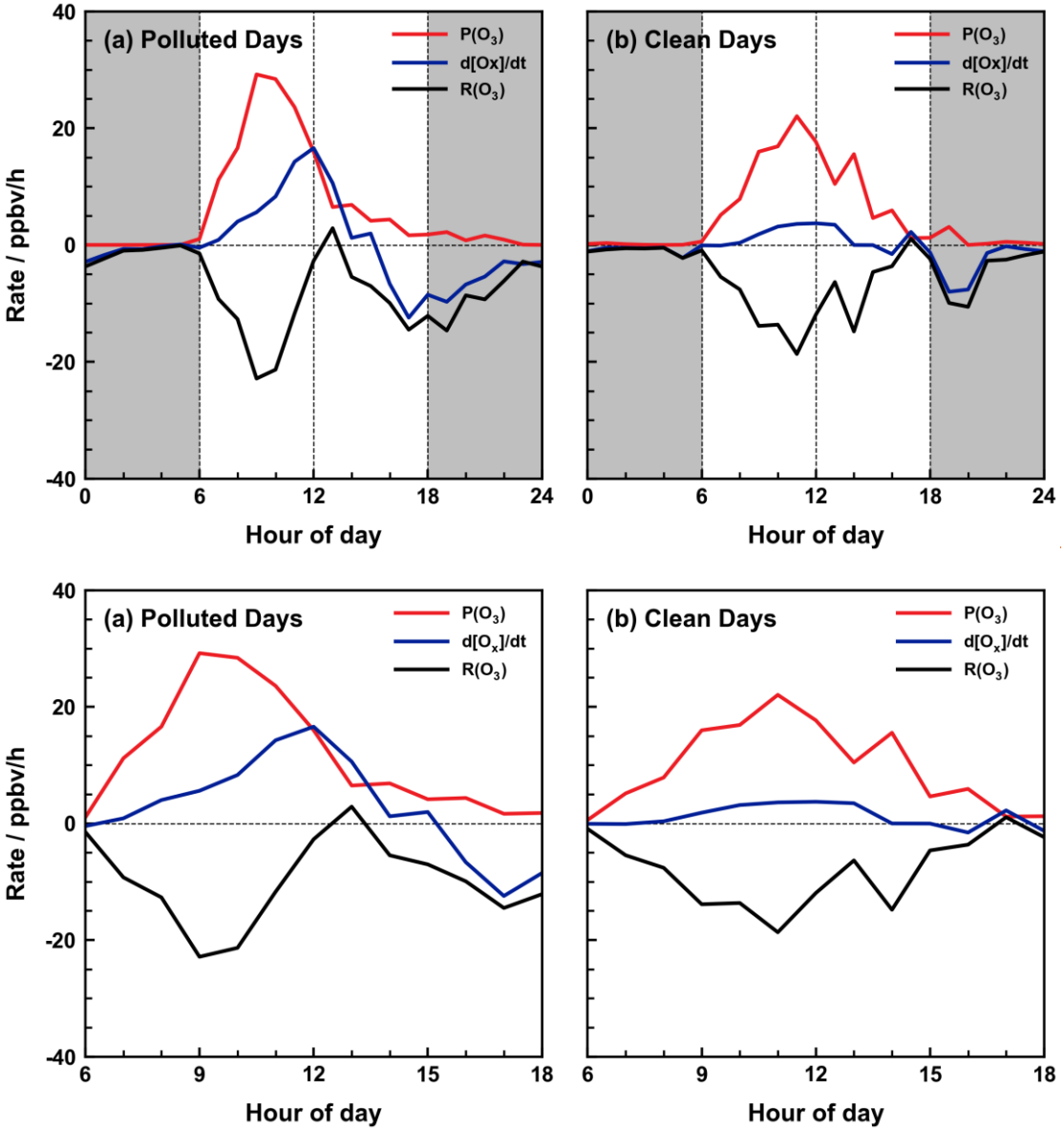

Figure 6. Diurnal variations of daytime $P(O_3)$, d[Ox]/dt, and $R(O_3)$ during (a) polluted and (b) clean periods. The red line represents the photochemical ozone production rate $P(O_3)$, the blue line indicates the rate of change of total oxidants d[Ox]/dt, and the black line corresponds to the regional transport rate $R(O_3)$. ~~The shaded areas (00:00–06:00 and 18:00–24:00) represent nighttime periods.~~

4. Conclusions

This study combined the PERCA technique with CEAS to develop a single-channel PERCA–CEAS system. The system enables real-time, online measurements of RO_2*, providing a robust technical support for evaluating atmospheric oxidation capacity and elucidating tropospheric photochemical mechanisms. Experimental investigations were conducted to determine key parameters affecting measurement performance. The detection limit for RO_2* was 0.~~2~~38 pptv (1σ) at a time resolution of 3 min, with an overall measurement uncertainty of ~~12–17~~18.4-25.7%, demonstrating high sensitivity and stability that meet the requirements for field observations of ambient RO_2*. Our PERCA–CEAS system was successfully deployed for ambient measurement and found moderate RO_2* levels in a coastal area. The $P(O_3)$ derived from measured RO_2* ~~is~~was further used to evaluate the O_3 formation regime and transport influence on O_3. The higher O_3 levels observed on polluted days compared to clean days were driven by both stronger photochemical production and reduced export effects during midday in this coastal area. Our study, therefore, provides an important reference for extending the peroxy radical measurement techniques to quantify in-situ formation and transport of O_3. We also suggest more field observations of peroxy radicals in diverse environments to support the strategy formulation of O_3 pollution.

Data availability. The dataset is available at https://doi.org/10.5281/zenodo.18346203 (Tang et al., 2026).

Author Contributions Statement. X.R.C. and H.C.W. conceived the study. R.J.T., and Z.L.Z., H.C.W. and X.R.C. analyzed the data and wrote the manuscript. R.J.T., Z.L.Z. set up the instrument and conducted the field experiment with the help of H.X.L. and Y.M.W. All authors contributed to the results and commented on the manuscript.

Competing Interests Statement. The authors declare no competing interests.

Acknowledgments. H.C.W. received financial support from the National Key Research and Development Program of China (2023YFC3710900), and the Guangdong Natural Science Funds for Distinguished Young Scholar (2024B1515020075). X.R.C received financial support from the National Natural Science Foundation of China (No. 22576242).

References

Anderson, D. C., Pavelec, J., Daube, C., Herndon, S. C., Knighton, W. B., Lerner, B. M., Roscioli, J. R., Yacovitch, T. I., and Wood, E. C.: Characterization of ozone production in san antonio, texas, using measurements of total peroxy radicals, Atmospheric Chem. Phys., 19, 2845–2860, https://doi.org/10.5194/acp-19-2845-2019, 2019.

Cantrell, C. A., Shetter, R. E., and Calvert, J.: Peroxy radical chemistry during FIELDVOC 1993 in brittany, france, Atmos. Environ., 30, 3947–3957, https://doi.org/10.1016/1352-2310(96)00136-7, 1996.

Chen, T., Zhang, P., Chu, B., Ma, Q., Ge, Y., Liu, J., and He, H.: Secondary organic aerosol formation from mixed volatile organic compounds: effect of RO2 chemistry and precursor concentration, Npj Clim. Atmospheric Sci., 5, 95–103, https://doi.org/10.1038/s41612-022-00321-y, 2022.

Chen, Y., Yang, C., Zhao, W., Fang, B., Xu, X., Gai, Y., Lin, X., Chen, W., and Zhang, W.: Ultra-sensitive measurement of peroxy radicals by chemical amplification broadband cavity-enhanced spectroscopy, Analyst, 141, 5870–5878, https://doi.org/10.1039/C6AN01038E, 2016.

Duncianu, M., Lahib, A., Tomas, A., Stevens, P. S., and Dusanter, S.: Characterization of a chemical amplifier for peroxy radical measurements in the atmosphere, Atmos. Environ., 222, 117106, https://doi.org/10.1016/j.atmosenv.2019.117106, 2020.

Edwards, G. D., Cantrell, C. A., Stephens, S., Hill, B., Goyea, O., Shetter, R. E., Mauldin, R. L., Kosciuch, E., Tanner, D. J., and Eisele, F. L.: Chemical ionization mass spectrometer instrument for the measurement of tropospheric HO_2 and RO_2, Anal. Chem., 75, 5317–5327, https://doi.org/10.1021/ac034402b, 2003.

Ehn, M., Thornton, J. A., Kleist, E., Sipilä, M., Junninen, H., Pullinen, I., Springer, M., Rubach, F., Tillmann, R., Lee, B., Lopez-Hilfiker, F., Andres, S., Acir, I.-H., Rissanen, M., Jokinen, T., Schobesberger, S., Kangasluoma, J., Kontkanen, J., Nieminen, T., Kurtén, T., Nielsen, L. B., Jørgensen, S., Kjaergaard, H. G., Canagaratna, M., Maso, M. D., Berndt, T., Petäjä, T., Wahner, A., Kerminen, V.-M., Kulmala, M., Worsnop, D. R., Wildt, J., and Mentel, T. F.: A large source of low-volatility secondary organic aerosol, Nature, 506, 476–479, https://doi.org/10.1038/nature13032, 2014.

Gao, Y., Lu, K., and Zhang, Y.: Review of technologies and their applications for the speciated detection of RO2 radicals, J. Environ. Sci., 123, 487–499, https://doi.org/10.1016/j.jes.2022.09.028, 2023.

George, M., Andrés Hernández, M. D., Nenakhov, V., Liu, Y., and Burrows, J. P.: Airborne measurement of peroxy radicals using chemical amplification coupled with cavity ring-down spectroscopy: the PeRCEAS instrument, Atmosp

heric Meas. Tech., 13, 2577–2600, https://doi.org/10.5194/amt-13-2577-2020, 2020.
Green, T. J., Reeves, C. E., Brough, N., Edwards, G. D., Monks, P. S., and Penkett, S. A.: Airborne measurements of peroxy radicals using the PERCA technique, J. Environ. Monit., 5, 75–83, https://doi.org/10.1039/b204493e, 2003.
Griffith, S. M., Hansen, R. F., Dusanter, S., Michoud, V., Gilman, J. B., Kuster, W. C., Veres, P. R., Graus, M., De Gouw, J. A., Roberts, J., Young, C., Washenfelder, R., Brown, S. S., Thalman, R., Waxman, E., Volkamer, R., Tsai, C., Stutz, J., Flynn, J. H., Grossberg, N., Lefer, B., Alvarez, S. L., Rappenglueck, B., Mielke, L. H., Osthoff, H. D., and Stevens, P. S.: Measurements of hydroxyl and hydroperoxy radicals during CalNex-LA: model comparisons and radical budgets, J. Geophys. Res. Atmospheres, 121, 4211–4232, https://doi.org/10.1002/2015JD024358, 2016.
Hornbrook, R. S., Crawford, J. H., Edwards, G. D., Goyea, O., Mauldin Iii, R. L., Olson, J. S., and Cantrell, C. A.: Measurements of tropospheric HO_2 and RO_2 by oxygen dilution modulation and chemical ionization mass spectrometry, Atmospheric Meas. Tech., 4, 735–756, https://doi.org/10.5194/amt-4-735-2011, 2011.
Horstjann, M., Andrés Hernández, M. D., Nenakhov, V., Chrobry, A., and Burrows, J. P.: Peroxy radical detection for airborne atmospheric measurements using absorption spectroscopy of NO_2, Atmospheric Meas. Tech., 7, 1245–1257, https://doi.org/10.5194/amt-7-1245-2014, 2014.
Kartal, D., Andrés-Hernández, M. D., Reichert, L., Schlager, H., and Burrows, J. P.: Technical note: characterisation of a DUALER instrument for the airborne measurement of peroxy radicals during AMMA 2006, Atmospheric Chem. Phys., 10, 3047–3062, https://doi.org/10.5194/acp-10-3047-2010, 2010.
Liang, W., Yu, H., Xu, H., Wang, Z., Li, T., Feng, Y., Russell, A., and Shi, G.: Probing into ozone production through photochemistry of organic peroxyl radicals: implications for source control, J. Geophys. Res. Atmospheres, 129, e2023JD040124, https://doi.org/10.1029/2023JD040124, 2024.
Liu, Y. and Zhang, J.: Atmospheric peroxy radical measurements using dual-channel chemical amplification cavity ringdown spectroscopy, Anal. Chem., 86, 5391–5398, https://doi.org/10.1021/ac5004689, 2014.
Liu, Y., Morales-Cueto, R., Hargrove, J., Medina, D., and Zhang, J.: Measurements of peroxy radicals using chemical amplification-cavity ringdown spectroscopy, Environ. Sci. Technol., 43, 7791–7796, https://doi.org/10.1021/es901146t, 2009.
Lou, S., Tan, Z., Gan, G., Chen, J., Wang, H., Gao, Y., Huang, D., Huang, C., Li, X., Song, R., Wang, H., Wang, M., Wang, Q., Wu, Y., and Huang, C.: Observation based study on atmospheric oxidation capacity in shanghai during late-autumn: contribution from nitryl chloride, Atmos. Environ., 271, 118902, https://doi.org/10.1016/j.atmosenv.2021.118902, 2022.

Lu, K. D., Rohrer, F., Holland, F., Fuchs, H., Bohn, B., Brauers, T., Chang, C. C., Häseler, R., Hu, M., Kita, K., Kondo, Y., Li, X., Lou, S. R., Nehr, S., Shao, M., Zeng, L. M., Wahner, A., Zhang, Y. H., and Hofzumahaus, A.: Observation and modelling of OH and HO_2 concentrations in the pearl river delta 2006: a missing OH source in a VOC rich atmosphere, Atmospheric Chem. Phys., 12, 1541–1569, https://doi.org/10.5194/acp-12-1541-2012, 2012.

Ma, X., Tan, Z., Lu, K., Yang, X., Liu, Y., Li, S., Li, X., Chen, S., Novelli, A., Cho, C., Zeng, L., Wahner, A., and Zhang, Y.: Winter photochemistry in beijing: observation and model simulation of OH and HO2 radicals at an urban site, Sci. Total Environ., 685, 85–95, https://doi.org/10.1016/j.scitotenv.2019.05.329, 2019.

Ma, X., Tan, Z., Lu, K., Yang, X., Chen, X., Wang, H., Chen, S., Fang, X., Li, S., Li, X., Liu, J., Liu, Y., Lou, S., Qiu, W., Wang, H., Zeng, L., and Zhang, Y.: OH and HO_2 radical chemistry at a suburban site during the EXPLORE-YRD campaign in 2018, Atmospheric Chem. Phys., 22, 7005–7028, https://doi.org/10.5194/acp-22-7005-2022, 2022.

Michoud, V., Kukui, A., Camredon, M., Colomb, A., Borbon, A., Miet, K., Aumont, B., Beekmann, M., Durand-Jolibois, R., Perrier, S., Zapf, P., Siour, G., Ait-Helal, W., Locoge, N., Sauvage, S., Afif, C., Gros, V., Furger, M., Ancellet, G., and Doussin, J. F.: Radical budget analysis in a suburban european site during the MEGAPOLI summer field campaign, Atmospheric Chem. Phys., 12, 11951–11974, https://doi.org/10.5194/acp-12-11951-2012, 2012.

Mihelcic, D., Müsgen, P., and Ehhalt, D. H.: An improved method of measuring tropospheric NO2 and RO2 by matrix isolation and electron spin resonance, J. Atmospheric Chem., 3, 341–361, https://doi.org/10.1007/BF00122523, 1985.

Mihelcic, D., Volz-Thomas, A., Pätz, H. W., Kley, D., and Mihelcic, M.: Numerical analysis of ESR spectra from atmospheric samples, J. Atmospheric Chem., 11, 271–297, https://doi.org/10.1007/BF00118353, 1990.

Mihele, C. M., Mozurkewich, M., and Hastie, D. R.: Radical loss in a chain reaction of CO and NO in the presence of water: implications for the radical amplifier and atmospheric chemistry, Int. J. Chem. Kinet., 31, 145–152, https://doi.org/10.1002/(SICI)1097-4601(1999)31:2%~~253C145~~3C145::AID-KIN7%~~253E33~~3E3.0.CO;2-M, 1999.

Monks, P. S.: Gas-phase radical chemistry in the troposphere, Chem. Soc. Rev., 34, 376, https://doi.org/10.1039/b307982c, 2005.

Orlando, J. J. and Tyndall, G. S.: Laboratory studies of organic peroxy radical chemistry: an overview with emphasis on recent issues of atmospheric significance, Chem. Soc. Rev., 41, 6294, https://doi.org/10.1039/c2cs35166h, 2012.

Reichert, L., Andrés Hernández, M. D., Stöbener, D., Burkert, J., and Burrows, J. P.: Investigation of the effect of water complexes in the determination of peroxy radical ambient concentrations: implications for the atmosphere, J. G

eophys. Res. Atmospheres, 108, https://doi.org/10.1029/2002JD002152, 2003.
Situ, S., Guenther, A., Wang, X., Jiang, X., Turnipseed, A., Wu, Z., Bai, J., and Wang, X.: Impacts of seasonal and regional variability in biogenic VOC emissions on surface ozone in the pearl river delta region, china, Atmospheric Chem. Phys., 13, 11803–11817, https://doi.org/10.5194/acp-13-11803-2013, 2013.
Sommariva, R., Brown, S. S., Roberts, J. M., Brookes, D. M., Parker, A. E., Monks, P. S., Bates, T. S., Bon, D., De Gouw, J. A., Frost, G. J., Gilman, J. B., Goldan, P. D., Herndon, S. C., Kuster, W. C., Lerner, B. M., Osthoff, H. D., Tucker, S. C., Warneke, C., Williams, E. J., and Zahniser, M. S.: Ozone production in remote oceanic and industrial areas derived from ship based measurements of peroxy radicals during TexAQS 2006, https://doi.org/10.5194/acpd-10-23109-2010, 7 October 2010.
Stone, D., Evans, M. J., Commane, R., Ingham, T., Floquet, C. F. A., McQuaid, J. B., Brookes, D. M., Monks, P. S., Purvis, R., Hamilton, J. F., Hopkins, J., Lee, J., Lewis, A. C., Stewart, D., Murphy, J. G., Mills, G., Oram, D., Reeves, C. E., and Heard, D. E.: HO_x observations over west Africa during AMMA: impact of isoprene and NO_x, Atmospheric Chem. Phys., 10, 9415–9429, https://doi.org/10.5194/acp-10-9415-2010, 2010.
Sun, J., Yu, X., Ling, Z., Fang, G., Ming, L., Zhao, J., Zou, S., Guan, H., Wang, H., Wang, X., Wang, Z., Gao, Y., Tham, Y. J., Guo, H., and Zhang, Y.: Roles of photochemical consumption of VOCs on regional background O3 concentration and atmospheric reactivity over the pearl river estuary, southern China, Sci. Total Environ., 928, 172321, https://doi.org/10.1016/j.scitotenv.2024.172321, 2024.
Tan, Z., Fuchs, H., Lu, K., Hofzumahaus, A., Bohn, B., Broch, S., Dong, H., Gomm, S., Häseler, R., He, L., Holland, F., Li, X., Liu, Y., Lu, S., Rohrer, F., Shao, M., Wang, B., Wang, M., Wu, Y., Zeng, L., Zhang, Y., Wahner, A., and Zhang, Y.: Radical chemistry at a rural site (wangdu) in the north China plain: observation and model calculations of OH, HO_2 and RO_2 radicals, Atmospheric Chem. Phys., 17, 663–690, https://doi.org/10.5194/acp-17-663-2017, 2017.
Tan, Z., Lu, K., Dong, H., Hu, M., Li, X., Liu, Y., Lu, S., Shao, M., Su, R., Wang, H., Wu, Y., Wahner, A., and Zhang, Y.: Explicit diagnosis of the local ozone production rate and the ozone-NOx-VOC sensitivities, Sci. Bull., 63, 1067–1076, https://doi.org/10.1016/j.scib.2018.07.001, 2018a.
Tan, Z., Rohrer, F., Lu, K., Ma, X., Bohn, B., Broch, S., Dong, H., Fuchs, H., Gkatzelis, G. I., Hofzumahaus, A., Holland, F., Li, X., Liu, Y., Liu, Y., Novelli, A., Shao, M., Wang, H., Wu, Y., Zeng, L., Hu, M., Kiendler-Scharr, A., Wahner, A., and Zhang, Y.: Wintertime photochemistry in beijing: observations of RO_x radical concentrations in the north China plain during the BEST-ONE campaign, Atmospheric Chem. Phys., 18, 12391–12411, https://doi.

org/10.5194/acp-18-12391-2018, 2018b.
Tan, Z., Lu, K., Hofzumahaus, A., Fuchs, H., Bohn, B., Holland, F., Liu, Y., Rohrer, F., Shao, M., Sun, K., Wu, Y., Zeng, L., Zhang, Y., Zou, Q., Kiendler-Scharr, A., Wahner, A., and Zhang, Y.: Experimental budgets of OH, HO_2, and RO_2 radicals and implications for ozone formation in the pearl river delta in China 2014, Atmospheric Chem. Phys., 19, 7129–7150, https://doi.org/10.5194/acp-19-7129-2019, 2019.
Tan, Z., Ma, X., Lu, K., Jiang, M., Zou, Q., Wang, H., Zeng, L., and Zhang, Y.: Direct evidence of local photochemical production driven ozone episode in beijing: a case study, Sci. Total Environ., 800, 148868, https://doi.org/10.1016/j.scitotenv.2021.148868, 2021.
Tang, R., Zheng, Z., and Chen, X.: Measurement report: development of a portable peroxy radical measurement system, https://doi.org/10.5281/ZENODO.18346203, 2026.
Thornton, J. A., Wooldridge, P. J., Cohen, R. C., Martinez, M., Harder, H., Brune, W. H., Williams, E. J., Roberts, J. M., Fehsenfeld, F. C., Hall, S. R., Shetter, R. E., Wert, B. P., and Fried, A.: Ozone production rates as a function of NO_x abundances and HO_x production rates in the nashville urban plume, J. Geophys. Res. Atmospheres, 107, https://doi.org/10.1029/2001JD000932, 2002.
Wang, H., Liu, Y., Chen, X., Gao, Y., Qiu, W., Jing, S., Wang, Q., Lou, S., Edwards, P. M., Huang, C., and Lu, K.: Unexpected fast radical production emerges in cool seasons: implications for ozone pollution control, Natl. Sci. Open, 1, 20220013, https://doi.org/10.1360/nso/20220013, 2022.
Wang, H., Wang, H., Lu, X., Lu, K., Zhang, L., Tham, Y. J., Shi, Z., Aikin, K., Fan, S., Brown, S. S., and Zhang, Y.: Increased night-time oxidation over China despite widespread decrease across the globe, Nat. Geosci., 16, 217–223, https://doi.org/10.1038/s41561-022-01122-x, 2023a.
Wang, J., Zhang, Y., Zhao, W., Wu, Z., Luo, S., Zhang, H., Zhou, H., Song, W., Zhang, W., and Wang, X.: Observationally constrained modeling of peroxy radical during an ozone episode in the pearl river delta region, china, J. Geophys. Res. Atmospheres, 128, e2022JD038279, https://doi.org/10.1029/2022JD038279, ~~2023~~2023b.
Wang, J., Zhang, Y., Xiao, S., Wu, Z., and Wang, X.: Ozone formation at a suburban site in the pearl river delta region, china: role of biogenic volatile organic compounds, Atmosphere, 14, 609–625, https://doi.org/10.3390/atmos14040609, 2023c.
Wei, N., Zhao, W., Yao, Y., Wang, H., Liu, Z., Xu, X., Rahman, M., Zhang, C., Fittschen, C., and Zhang, W.: Peroxy radical chemistry during ozone photochemical pollution season at a suburban site in the boundary of jiangsu–anhui–shandong–henan region, china, Sci. Total Environ., 904, 166355, https://doi.org/10.1016/j.scitotenv.2023.166355, 2023.

Whalley, L. K., Blitz, M. A., Desservettaz, M., Seakins, P. W., and Heard, D. E.: Reporting the sensitivity of laser-induced fluorescence instruments used for HO_2 detection to an interference from RO_2 radicals and introducing a novel approach that enables HO_2 and certain RO_2 types to be selectively measured, Atmospheric Meas. Tech., 6, 3425–3440, https://doi.org/10.5194/amt-6-3425-2013, 2013.

Wolfe, G. M., Marvin, M. R., Roberts, S. J., Travis, K. R., and Liao, J.: The framework for 0-D atmospheric modeling (F0AM) v3.1, Geosci. Model Dev., 9, 3309–3319, https://doi.org/10.5194/gmd-9-3309-2016, 2016.

Wood, E. C. and Charest, J. R.: Chemical amplification - cavity attenuated phase shift spectroscopy measurements of atmospheric peroxy radicals, Anal. Chem., 86, 10266–10273, https://doi.org/10.1021/ac502451m, 2014.

Wood, E. C., Deming, B. L., and Kundu, S.: Ethane-based chemical amplification measurement technique for atmospheric peroxy radicals, Environ. Sci. Technol. Lett., 4, 15–19, https://doi.org/10.1021/acs.estlett.6b00438, 2017.

Yang, C., Zhao, W., Fang, B., Yu, H., Xu, X., Zhang, Y., Gai, Y., Zhang, W., Chen, W., and Fittschen, C.: Improved chemical amplification instrument by using a nafion dryer as an amplification reactor for quantifying atmospheric peroxy radicals under ambient conditions, Anal. Chem., 91, 776–779, https://doi.org/10.1021/acs.analchem.8b04907, 2019.

Yang, X., Lu, K., Ma, X., Gao, Y., Tan, Z., Wang, H., Chen, X., Li, X., Huang, X., He, L., Tang, M., Zhu, B., Chen, S., Dong, H., Zeng, L., and Zhang, Y.: Radical chemistry in the pearl river delta: observations and modeling of OH and HO_2 radicals in shenzhen in 2018, Atmospheric Chem. Phys., 22, 12525–12542, https://doi.org/10.5194/acp-22-12525-2022, 2022.

Yu, H., Wei, N. N., Xu, X. Z., Liu, Q. Q., Yao, Y. C., Zhao, W. X., and Zhang, W. J.: Characteristics of Summer O3 Formation in the Western Suburbs of Hefei Based on Total Peroxy Radical Observations, Environ. Sci., 44, 1974–1984, https://doi.org/10.13227/j.hjkx.202206116, 2023 (in Chinese).

Zhang, G., Hu, R., Xie, P., Hu, C., Liu, X., Zhong, L., Cai, H., Zhu, B., Xia, S., Huang, X., Li, X., and Liu, W.: Intensive photochemical oxidation in the marine atmosphere: evidence from direct radical measurements, https://doi.org/10.5194/egusphere-2023-550, 19 June 2023.

Zheng, Z., Wang, H., Chen, X., Wang, J., Li, X., Lu, K., Yu, G.-H., Huang, X., and Fan, S.: A mini broadband cavity enhanced absorption spectrometer for nitrogen dioxide measurement on the unmanned aerial vehicle platform, Atmos. Environ., 321, 120361, https://doi.org/10.1016/j.atmosenv.2024.120361, 2024.

Zou, Z., Chen, T., Chen, Q., Sun, W., Han, S., Ren, Z., Li, X., Song, W., Ge, A., Wang, Q., Tian, X., Pei, C., Wang, X., Zhang, Y., and Wang, T.: Observation and modeling of atmospheric OH and HO_2^* radicals at a subtropical rural site and implications for secondary pollutants, Atmospheric Chem. Phys.,

25, 8147–8161, https://doi.org/10.5194/acp-25-8147-2025, 2025.